Numerical Resolution of Some Nonlinear Schrödinger-Like Equations in Plasmas

C.–H. Bruneau,[1] **L. Di Menza,**[2] **T. Lehner**[3]

[1] *Mathématiques Appliquées de Bordeaux*
Université Bordeaux I
33405 Talence Cedex, France

[2] *Analyse numérique et EDP*
Université Paris-Sud
91405 Orsay Cedex, France

[3] *CNRS, UPR 287 SPI*
P.M.I., Ecole Polytechnique
91128 Palaiseau, France

Received April 4, 1998; accepted November 27, 1998

Schrödinger-like equations play an essential role in the modeling of plasmas created by laser beams, and taking into account of relativistic terms yields a new kind of nonlinearity in them, as compared to the classical case. A numerical scheme involving a new handling of absorbing conditions suitable for Schrödinger-like equations is given, and several general models are studied: the classical cubic case linked to the Kerr effect for an anharmonic plasma, where numerical experiments prove the efficiency of our code applied to the computation of solitons and explosive solutions. Furthermore, new kinds of explosive solutions are computed, and we numerically show the essential role of the ground state to get approximations of the cubic explosive solution by global ones. A multiphotonic ionization model is also studied including higher-order terms in the nonlinearity. In this case, we obtain stable structures physically explained by competing saturation processes. These structures have been experimentally detected. Finally, a relativistic model involving the Lorentz kinematic factor in the evolution equations is investigated numerically; filamentary structures are found in agreement with predicted relativistic phenomena. Numer Methods Partial Differential Eq 15: 672–696, 1999

Keywords: finite differences schemes; absorbing conditions; nonlinear Schrödinger equations; relativistic models

I. INTRODUCTION

Our aim in this article is to investigate solutions for physical systems described by the help of nonlinear partial differential equations. We focus on equations of the nonlinear Schrödinger

Correspondence to: L. Di Menza
 CCC 0749-159X/99/060672-25

type, relevant especially for plasma physics in the context of laser–matter interaction. We look for coherent structures resulting from the propagation of a laser beam within a plasma. The complexity of such systems requires numerical analysis. However, the handling of boundary conditions turns out to be an important issue in these problems.

In this work, we use previously designed absorbing boundary conditions (see [1, 2]) suitable for solving the equations under study. We start with the classical cubic nonlinear equation to valid our numerical simulation. Then we study modified equations that arise in the context of short laser pulses in interaction with matter, particularly in the relativistic regime at high laser intensities. The equations are derived with the slow space and time envelope approximation implying well-separated time and space scales.

The outline of this paper is the following: in Section II, we summarize the numerical scheme used, emphasizing the importance of the boundary conditions and we illustrate it in the simplest case: the one-dimensional linear Schrödinger equation. In Section III, we apply our tests to the cubic nonlinear Schrödinger equation (NLS) recovering the usual features for this equation: critical power, blow-up, solitary waves, and stationary solutions. The computations give numerical solutions with a prescribed blow-up time in agreement with self-similar theory (see [3]). Then we switch to more complex systems of physical relevance. In Section IV, we examine a modified NLS equation. New nonlinearities are justified on physical arguments given in the introduction of this section. This modified Schrödinger-like equation arises in the case of moderate laser intensities ($I \leq 10^{15}$ W/cm^2) for which the formation of optical light bullets may occur. We solve this equation and find self-guided solutions that are experimentally observed ([4]). In addition, we discuss the behavior of the solution depending on various physical parameters to be discussed. In Section V, we consider the relativistic regime ($I \geq 10^{18}$ W/cm^2) and we rederive the coupled nonlinear equations for the electronic density n and the vector potential from Maxwell equations, together with relativistic hydrodynamics that are responsible in particular for the relativistic self-focusing ([6, 8–11, 35]). In particular, we restrict our attention to the so-called relativistic nonlinear Schrödinger equation that is obtained in the framework of the adiabatic approximation. There, stationary solutions could also be obtained. They correspond to stable and localized structures for the laser beam that have been theoretically predicted ([9]) and also observed ([8, 12]). We introduce here azimuthal perturbation in the spirit of [9] in order to test the stability of the solutions, and filamentary structures can indeed be observed.

II. NUMERICAL METHOD AND ILLUSTRATION FOR THE LINEAR CASE

In this section, we introduce the numerical method used to compute solutions of Schrödinger-type equations in a bounded bidimensional space domain. In all the following, space and time variables are labeled, respectively, $x = (x_1, x_2)$ and t.

A. Numerical Scheme

The resolution is made by using a Crank–Nicolson implicit finite differences scheme. Starting from the general Schrödinger equation

$$i\partial_t E + \Delta_{x_1,x_2} E + g(|E|)E = 0, \qquad E \in C, \tag{1}$$

we compute the value of the electric field E at a finite number of grid points corresponding to space steps $\Delta x_1, \Delta x_2$, and at finite successive times $t_n = n\Delta t$ $(n = 0, 1, 2, \ldots)$. Denoting by $E^n_{j,k}$ the value of E at the point $(j\Delta x_1, k\Delta x_2)(j = 0, \pm 1, \ldots, k = 0, \pm 1, \ldots)$ at time t_n, we

make an approximation of the differential terms leading to a discrete system. We thus introduce the second-order finite differences discretization operators

$$\begin{aligned} L_x E^n_{j,k} &= (E^n_{j+1,k} - 2E^n_{j,k} + E^n_{j-1,k})/\Delta x_1^2 \\ L_y E^n_{j,k} &= (E^n_{j,k+1} - 2E^n_{j,k} + E^n_{j,k-1})/\Delta x_2^2, \end{aligned}$$

and we set $E^{n+1/2}_{j,k} = (E^n_{j,k} + E^{n+1}_{j,k})/2$. Discretization of Eq. (1) leads to the following equation (see [13]):

$$\frac{i}{\Delta t}\,(E^{n+1}_{j,k} - E^n_{j,k}) + (L_x + L_y)E^{n+1/2}_{j,k} + h(E^{n+1}_{j,k}, E^n_{j,k})E^{n+1/2}_{j,k} = 0, \tag{2}$$

where h is chosen in such a way that the two discrete invariants of (1) are preserved. In the special case

$$g(x) = \sum_{j=1}^{N} \alpha_j x^{2j},$$

we have

$$h(x,y) = \sum_{j=1}^{N} \frac{\alpha_j}{j+1} \sum_{k=0}^{j} x^{2j} y^{2(k-j)}.$$

This discretization enables us to find a discrete nonlinear system that we solve with a fixed-point algorithm: noting U^n the vector of the approximate solution considered for all the spatial points at time t_n, the system can be written in the following form:

$$M_+ U^{n+1} = M_- U^n + K(U^n, U^{n+1}),$$

where K stands for the nonlinear contribution, and matrices $M_\pm$ come from the discretization of the linear terms. Then, we define the sequence $(W_l)_{n\geq 0}$ with

$$\begin{cases} W_0 = U^n, \\ M_+ W_{l+1} = M_- U^n + K(U^n, W_l) \qquad l \geq 0. \end{cases}$$

The computation of $(W_l)_{n\geq 0}$ requires only linear inversions. Furthermore, since this sequence converges to U^{n+1} when $l \to \infty$, we stop this linear cycle as soon as the relative error

$$\epsilon_l = \frac{\|W_{l+1} - W_l\|_\infty}{\|W_1 - U^n\|_\infty}$$

becomes smaller than a prescribed value ϵ_0 (here, we always take $\epsilon_0 = 10^{-5}$, which gives an average number of 5 linear iterations).

B. Derivation of Transparent and Absorbing Conditions

The previous nonlinear system cannot be solved numerically, because we need a finite number of grid points and consequently a bounded computational domain. Considering Eq. (1) set in a spatial rectangular bounded domain Ω, we need to set conditions at the frontier that will not affect the evolution of E. Because of propagation effects in this type of equation, it is essential to choose nonreflecting conditions. In fact, transparent conditions seem to be the most appropriate, but they are very costly to compute due to their nonlocal form. These conditions have been introduced first for the wave equation in [14, 15], and later for parabolic problems [16]. Later,

approximate conditions have been derived [17–19]) in order to compute solutions with a low CPU time. Concerning Schrödinger equation, we have found transparent conditions in [1, 20] and also local conditions by means of approximation. Thus, we chose here absorbing boundary conditions, derived from the rational fraction approximation of the complex square root in the exact nonlocal transparent condition. We write transparent and absorbing boundary conditions for the Schrödinger two-dimensional case, and we compute the solution of the corresponding linear mixed problem. Then, we still extend their use to the cubic nonlinear case.

First, we give the expression of the transparent conditions for the linear Schrödinger equation

$$i\frac{\partial}{\partial t}u + \Delta u = 0, \qquad \Delta = \frac{\partial^2}{\partial x_1^2} + \frac{\partial^2}{\partial x_2^2}, \tag{3}$$

looking for a complex valued solution $u = u(t, x_1, x_2)$ in the half-plane $\Omega = \{(x_1, x_2) \in \mathbf{R}^2 / x_2 < 0\}$. Considering Fourier variables ω, K_1, K_2, respectively, associated to t, x_1, and x_2, the Schrödinger operator becomes

$$-(\omega + K_1^2 + K_2^2), \tag{4}$$

derivations being replaced by Fourier variable multiplications. Writing now

$$K_1^2 + K_2^2 + \omega = (K_2 + \sigma_1)(K_2 + \sigma_2), \tag{5}$$

and choosing the right operator σ_1 with condition $\mathcal{I}m(\sigma_1) < 0$ in order to preserve the right decreasing rate at infinity (see [1, 2]), one gets the following relation on the boundary:

$$\frac{\partial}{\partial x_2}u + \sigma u = 0 \text{ on } \Gamma, \tag{6}$$

where the symbol of σ is given by

$$\sigma(\omega, K_1) := e^{-i\pi/4}\sqrt{i\omega + iK_1^2}.$$

This is the expected transparent boundary condition. We clearly see that there is no interest in implementing it because of the high time computation for the solution of the mixed problem: the symbol of σ is not polynomial, and thus defines a nonlocal operator.

We find now simpler boundary conditions considering rational fraction approximation of the complex square root in Eq. (6). This method has given good numerical results in the case of the wave equation (see [17–19]) or the heat equation (see [16]). Instead of taking $(i\omega + iK_1^2)^{1/2}$, we choose $R_m(i\omega + iK_1^2)$, with

$$R_m(Z) = a_0 + \sum_{k=1}^{m} \frac{a_k Z}{Z + d_k}, \qquad a_k > 0, \qquad d_k > 0,$$

m being a nonnegative integer. The fraction R_m is chosen to interpolate exactly the complex square root at a finite family of points $\{\omega_0, (\pm i\omega_k)_{k=1,\ldots,m}\}$, computed in order to minimize the $L^2([0, \rho]_\omega)$-distance between R_m and $\sqrt{i\omega}$ (with $0 \le \omega_k \le \rho, k = 0, \ldots, m$). For a given m, we compute $\{a_k\}_{k=0,\ldots,m}, \{d_k\}_{k=1,\ldots,m}$, and $\{\omega_k\}_{k=0,\ldots,m}$ by successive one-dimensional minimizations (see [2, 16]). m is linked to the precision of approximation of the square root. Numerically, we see that the greater it is, the better R_m is for the L^2 norm. We give in Table I the values of these coefficients in the case $m = 6$.

Boundary condition (6) now takes the form

$$\frac{\partial}{\partial x_2}u + B_m u = 0 \text{ for } x_2 = 0, \tag{7}$$

TABLE I. Numerical values of (ω_k), (a_k), and (d_k) for $m = 6$.

k	ω_k	a_k	d_k
0	7.10^{-4}	$1.44\ 10^{-2}$	—
1	$6.04\ 10^{-3}$	3.23	7.06
2	$3.04\ 10^{-2}$	0.39	0.88
3	0.11	0.19	0.26
4	0.29	0.11	$7.84\ 10^{-2}$
5	0.59	$6.91\ 10^{-2}$	$1.88\ 10^{-2}$
6	0.9	$3.99\ 10^{-2}$	$2.92\ 10^{-3}$

where B_m is defined with Fourier variables $B_m(\omega, K_1) = e^{-i\pi/4} R_m(i\omega + iK_1^2)$. Boundary conditions (7) are already nonlocal, because the symbol of operator B_m is a rational fraction. In order to get local ones, we have to introduce at the boundary auxiliary quantities denoted by $\varphi_k(t, x)(k = 1, \ldots, m)$ satisfying

$$\frac{1}{i\omega + iK_1^2 + d_k} \hat{u} = \hat{\varphi}_k, \qquad k = 1, \ldots, m.$$

Multiplying by $i\omega + iK_1^2 + d_k$ enables us to find that in usual space, every φ_k satisfies a linear Schrödinger equation depending on u at the boundary:

$$i\frac{\partial}{\partial t}\varphi_k + \frac{\partial^2}{\partial x_1^2}\varphi_k + id_k\varphi_k = iu, \qquad k = 1, \ldots, m. \tag{8}$$

Boundary conditions (6) turn into

$$\begin{cases} \frac{\partial}{\partial x_2} u + e^{-i\pi/4} \left(\left(\sum_{k=0}^{m} a_k \right) u - \sum_{k=1}^{m} a_k d_k \varphi_k \right) = 0, & x_2 = 0 \\ i\frac{\partial}{\partial t}\varphi_k + \frac{\partial^2}{\partial x_1^2}\varphi_k + id_k\varphi_k = iu, & x_2 = 0, \qquad k = 1, \ldots, m. \end{cases} \tag{9}$$

To start the calculations, we choose $\varphi_k(0, x_1) = 0$ $(k = 1, \ldots, m)$. For more details about nonreflecting boundary conditions such as mathematical analysis or computation of the coefficients, see [1, 14, 15, 18–20].

In the case of a rectangular domain, each linear Schrödinger equation is also set on a bounded interval and also needs appropriate boundary conditions. In [2], we have developed two-level absorbing conditions with use of other auxiliary quantities $\psi_{k,l}$ for each φ_k. But numerical experiments have shown that this method does not give much better results than in the case where Dirichlet conditions are set at the boundary of the segment for φ_k. More precisely, if we consider an oblique pulse going through one of the corners, wall interactions arise. We have not yet found simple corner conditions, as in the case of the wave equation as in [17] because of the inhomogeneity of the Schrödinger symbol. But the size of the numerical box can be adapted in such a way that interaction effects are negligible.

Remark 2.1. It is not really precise to call conditions (9) local conditions. But the nonlocal aspect holds for functions φ_k defined on the surface, for which evolution is given by a classical Schrödinger equation at the boundary. Numerical methods such as finite difference schemes give efficient ways of solving (8). Therefore, boundary conditions (9) are simpler to compute.

Remark 2.2. In the one-dimensional case, the orthogonal contribution vanishes, and each φ_k satisfies a differential equation. Thus, we have $2m$ auxiliary quantities depending only on time to compute.

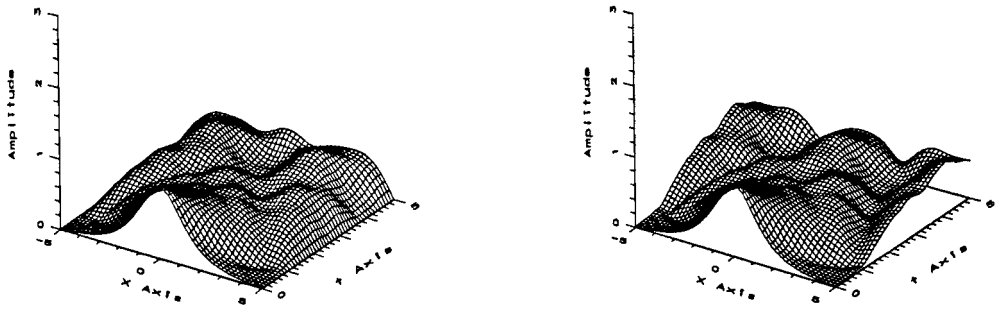

FIG. 1. Plot of the field, Dirichlet, and Neumann boundary conditions.

Remark 2.3. In [19], several kinds of approximations have been compared for the numerical resolution of the two-dimensional wave equation.

C. Influence of Boundary Conditions on the Numerical Solution

In this section, we numerically solve the Schrödinger equation in the simplest case: the one-dimensional linear homogeneous equation,

$$i\frac{\partial u}{\partial t} + \frac{\partial^2 u}{\partial x^2} = 0,$$

in the bounded domain $\Omega =]a, b[$. Our aim is to illustrate that, even in this linear situation, the treatment of the boundary is essential, since ill-adapted numerical conditions lead to a wrong approximate solution. We use here the Crank–Nicolson scheme described in Section II.A in the one-dimensional case, setting $g = 0$ (that is $h = 0$). Thus, we need only the inversion of a tridiagonal system during a time increment, because only one second-order derivation term is involved. We consider here Gaussian initial data $u_0(x) = \exp\{-x^2\}$, and we show in Figs. 1, 2, and 3, a (x, t)-plot of the field amplitude computed with different boundary conditions: Dirichlet conditions, Neumann conditions, absorbing conditions, and transparent conditions implemented as in [5], comparing them with the exact solution $u_{ex}(x, t) = \{\exp(-x^2/(1 + 4it))\}/\sqrt{1 + 4it}$. These computations have been performed on the bounded domain $]-5, 5[$ with time and space steps $\Delta t = 0.05, \Delta x = 0.1$, until the final time $T = 5$. Note that the use of absorbing conditions avoids the generation of artificial reflected waves at the numerical boundary.

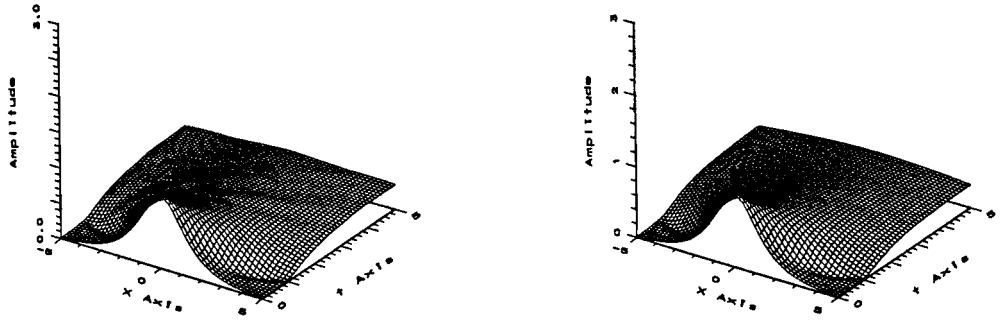

FIG. 2. Plot of the field, absorbing conditions ($m = 2$ and $m = 15$).

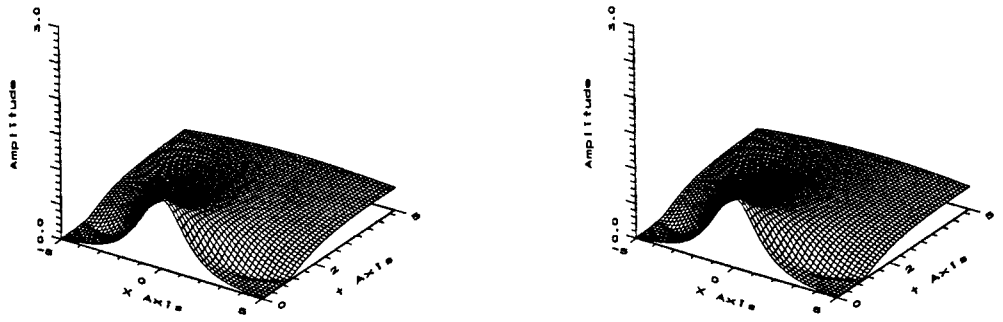

FIG. 3. Plot of the field, transparent conditions, and exact solution.

In order to compare more precisely the influence of the boundary conditions on the solution profile, we plot in Fig. 4 the evolution of $|u(t,0)|$ with respect to time, for the different simulations. This enables us to see that absorbing conditions preserve the decreasing rate of the solution, even if, for low values of m, small oscillations occur when $t > 5$.

The use of absorbing conditions avoids the generation of artificial reflecting waves caused by an ill-adapted treatment of the boundary. In this purely linear case, taking Dirichlet or Neumann conditions gives a wrong numerical solution, since the physical meaning of the boundary conditions is different: they do not match the free dispersion $\omega(k) = -k^2$ of the Gaussian beam.

We also made comparisons with other kinds of boundary conditions already used in order to avoid the problem of artificial reflections. A commonly used trick adds in the Schrödinger equation a term with support taken from around the boundary; the new equation thus becomes

$$i\frac{\partial E}{\partial t} + \frac{\partial^2 E}{\partial x^2} + i\gamma(x)E = 0, \tag{10}$$

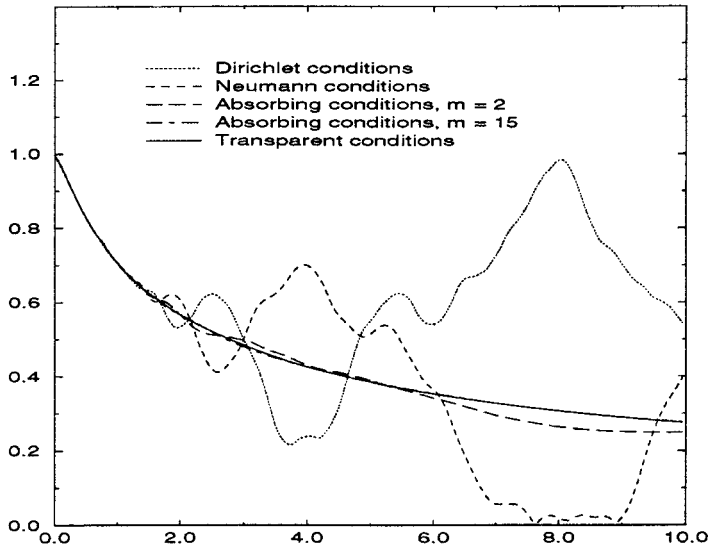

FIG. 4. Plot of the field at $x = 0$, different boundary conditions.

where we set $\gamma(x) = \operatorname{sech}^2(\max\{x - x_{\min}, x_{\max} - x\})$. This new term forces the stopping of the waves reaching the boundary neighborhood, which causes the vanishing of reflected beams through the segment's extremities.

Figure 5 shows both the (x, t)-plot of the field amplitude computed with this new equation and a comparison of the solution amplitude at the origin for absorbing conditions and for Eq. (10). We notice here that the absorbing conditions keep the decreasing rate of the exact solution, whereas the other solution gives birth to oscillations that propagate through the numerical domain. Furthermore, it is not obvious how to choose the right function γ for any initial data: this choice is, in fact, arbitrary. On the contrary, absorbing conditions come from a rigorous analysis of the Schrödinger problem. In what follows, we still use the finite-difference scheme without considerations of possible physical dispersion effects, since our conditions prevent artificial reflections from occurring.

In the next section, we use our numerical scheme for nonlinear equations in one-dimensional and two-dimensional geometries.

III. CUBIC NONLINEAR SCHRÖDINGER EQUATION

We are first interested in the computation of autofocusing phenomena that occur in nonlinear media. In a symmetric medium, the dominant nonlinearity in a power expansion into the electric field leads to a nonlinear index $n = n_0 + n_2|E|^2$; this is known as the Kerr nonlinearity. Modeling of a plasma with such index n together with the envelope approximation (see [21, 22]) leads to the following partial differential equation in 2D:

$$i\partial_t E + \Delta_{x_1,x_2} E = -|E|^2 E, \tag{11}$$

where E denotes the complex electric field, and the evolution parameter is given in the slowly varying amplitude approximation ([10, 22]). In some cases such as the one-dimensional cubic case, analytical solutions can be found by means of the inverse scattering method (see [23]). Furthermore, it is well known that solutions are global, and bounded in time.

A. One-Dimensional Cubic Equation

First, we compute the solution of (11) with the initial data $E_0(x) = i \exp 2ik_0 x / \cosh x$. Here, the solution of the Cauchy problem set in $\mathbf{R}$ takes the known explicit form obtained by using the

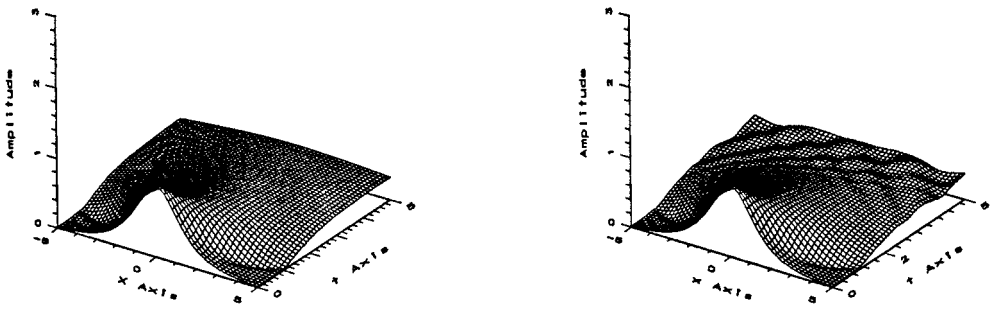

FIG. 5. Plot of the field, comparison with other boundary conditions.

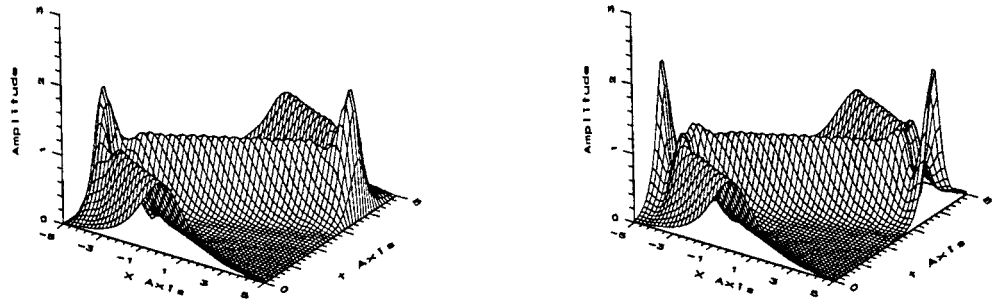

FIG. 6. Computation of a moving soliton with Dirichlet and Neumann conditions.

inverse scattering method (for more details about the resolution, see ([23]):

$$E(x,t) = i\frac{\exp i(2k_0x + (1-4k_0^2)t)}{\cosh(x-4k_0t)}.$$

Figures 6 and 7 view the plot of the amplitude $|E|$, respectively, computed with Dirichlet conditions ($E = 0$ for $x = x_{\min}$ and $x = x_{\max}$) and Neumann conditions ($\frac{\partial E}{\partial x} = 0$ for $x = x_{\min}$ and $x = x_{\max}$), and absorbing boundary conditions taken with $m = 5$ and $m = 15$. We point out that, in the first case, a strong reflection occurs at the right side of the domain, whereas the wave can go outside the domain using conditions (7) with very poor reflection. This case is a numerical demonstration of the efficiency of absorbing conditions even if they have been derived from the linear Schrödinger equation.

B. Two-Dimensional Cubic Equation

1. Validity of the Boundary Conditions in the Explosive Case. We use our code to solve the Schrödinger nonlinear cubic equation in the self-focusing case. We considered a moving gaussian beam for which its Hamiltonian is negative. Viriel identity grants the existence of a time T^* for which there is no more classical solution. We took here the following initial data:

$$u_0(x,y) = 3\exp\{-(x_1^2+x_2^2)\}\exp(ikx_1), \tag{12}$$

with $k = 10$: that means that the oscillating term forces the gaussian initial beam to travel to the right side of the domain. We made our computation in the space domain $]-3.5, 1.5[\times]-2.5, 2.5[$

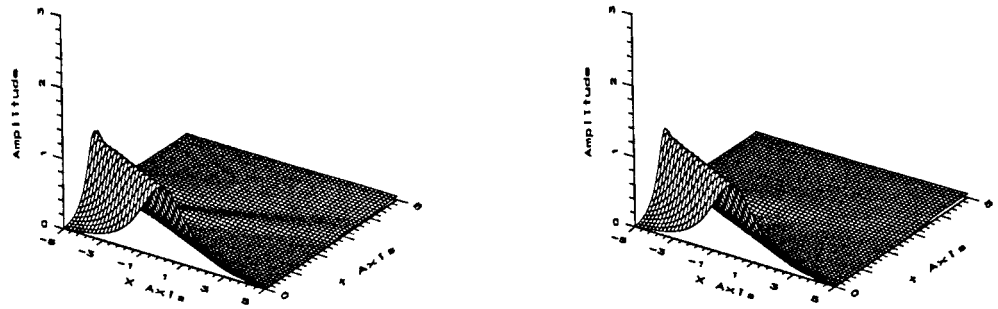

FIG. 7. Computation of a moving soliton with absorbing boundary conditions ($m = 5$, $m = 15$).

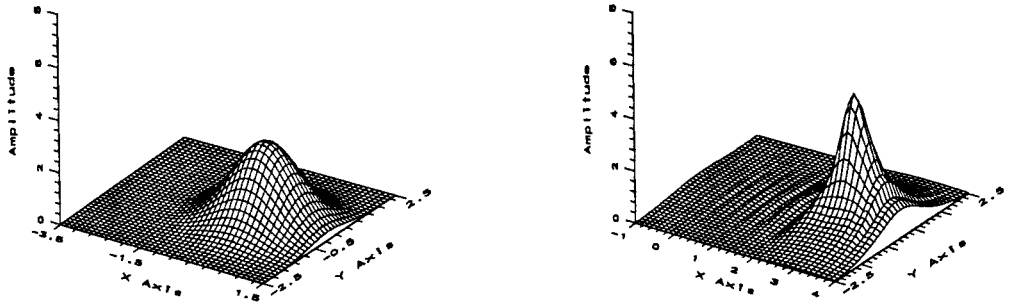

FIG. 8. Plot of the field, initial data, and ''nonperturbed'' solution at $t = 0.2$.

with $\Delta x_1 = \Delta x_2 = 0.125$ and $\Delta t = 0.0005$. We plot in Fig. 8 the initial amplitude and the amplitude of the field computed in a domain such that the solution support remains in the numerical domain at the final computation time (here, we took a gaussian initial function centered at the left side of the domain). In Fig. 9 are seen the plots of the field amplitude, respectively, computed with Neumann and Dirichlet conditions. In Fig. 10, we plot the amplitude of the solution computed with absorbing conditions taken for two different values of m ($m = 5$ and $m = 19$).

Here again, the use of absorbing conditions gives much better results than taking other kinds of boundary conditions. Nevertheless, a reflected wave traveling to the left remains. But we have to keep in mind that this test is a very severe one, since there is a pinching effect on the beam due to the focusing nonlinearity. Thus, it looks quite impossible to suppress the whole reflection at the boundary, since, for high concentration rates where the mesh turns out to become too coarse, finite-difference approximations do not lead to accurate numerical results. It would become more relevant in this precise situation to work with an adaptive mesh, as in [7].

2. Computation of Stationary Solutions. We are now interested in the computation of stationary solutions of Eq. (11), that is, to find solutions with an oscillatory time dependence: $E(t, x) = \exp(i\omega t)u(x)$. In this case, we get the nonlinear elliptic problem in $\mathbf{R}^2$

$$-\omega u + \Delta_{x_1,x_2} u + u^3 = 0, \tag{13}$$

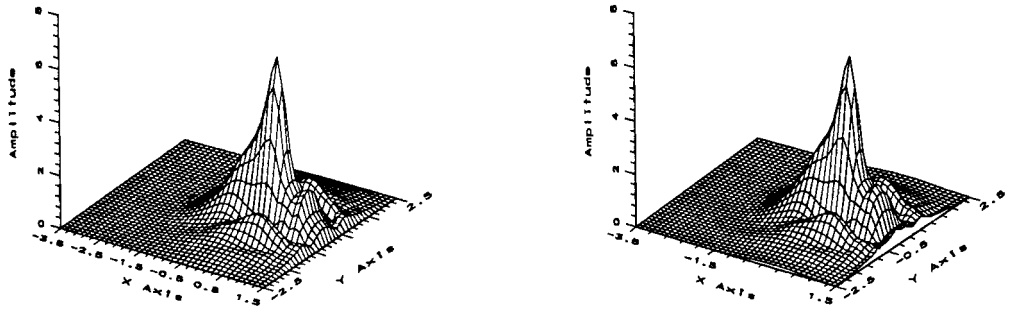

FIG. 9. Solution at $t = 0.2$, Dirichlet conditions and Neumann conditions.

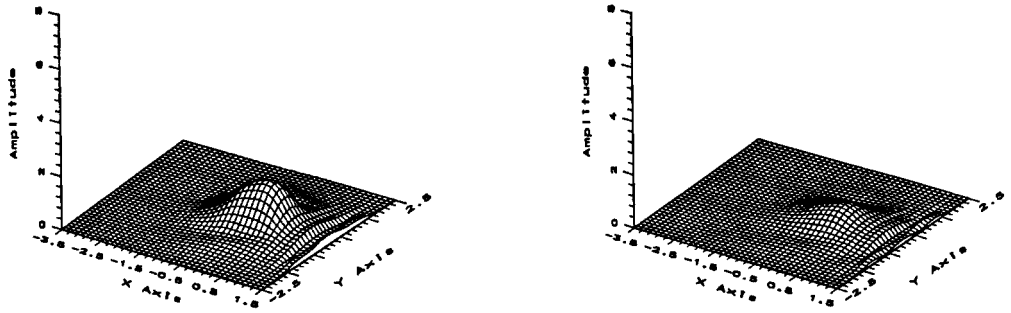

FIG. 10. Solution at $t = 0.2$, absorbing conditions ($m = 5$ and $m = 19$).

which cannot be solved directly with our numerical code. Furthermore, if we assume that u is radial $(u(x) = U(r), r = \|x\|)$, Eq. (13) reduces to a single ordinary differential equation:

$$\frac{1}{r}\frac{\partial}{\partial r}\left(r\frac{\partial}{\partial r}\right)U - \omega U + U^3 = 0. \tag{14}$$

We have to complete this equation by adding initial data. First, it is natural to set $\partial U/\partial r(0) = 0$, since U stands for an even function of r. Concerning the value of U at $r = 0$, Weinstein considered $U(0) = 2.2$ in [24] in order to find the unique positive radial solution Q_r with exponential decay at infinity. In fact, Q_r is called a ground state, and it plays an essential role for global existence of solutions for Eq. (11) (see [3, 25]).

3. Temporal Simulations with Stationary Profiles. We wish here to compute the ground state, and to inject it as the initial data in order to check the validity of our code. We used Maple V to numerically solve Eq. (14), and we chose $U(0) = 2.20617$, which enables us to get a positive solution with a correct decreasing rate until $r = 8$, which is sufficient for our simulations, since we work in a bounded domain. The space domain is $\Omega =]-5, 5[\times]-5, 5[$, with space steps $\Delta x_1 = \Delta x_2 = 0.2$, and time increment $\Delta t = 0.01$ s. In Fig. 11, we present the profile of the stationary state, and we compare the corresponding evolution at the center of Ω to solutions computed with the perturbation $(1+\epsilon)Q_r$, $(1-\epsilon)Q_r$ (here, $\epsilon = 0.05$). We see on Fig. 11 that multiplying the computed stationary state by $1+\epsilon$ leads to a blow-up of the corresponding

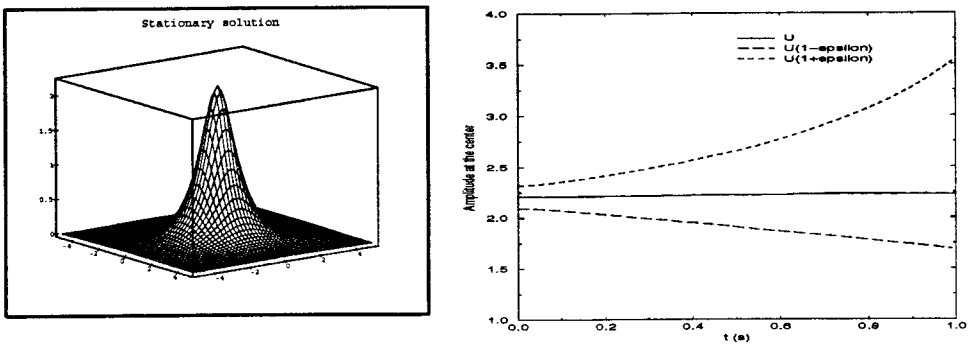

FIG. 11. Stationary profile and influence of amplitude perturbation.

solution, and, conversely, multiplying by $1-\epsilon$ yields a dispersive wave. This test gives a numerical illustration of the instability of stationary states for the cubic equation ([26]).

Computation of stationary states is essential, since it allows us to find explicit solutions of Eq. (11), with finite blow-up time: if $T > 0$, then

$$E(t, x_1, x_2) = \frac{1}{|T-t|} \exp\left\{ i \frac{1}{T-t} \right\} \exp\left\{ -\left(i \frac{x_1^2 + x_2^2}{4(T-t)} \right) \right\} Q_r\left(\frac{x_1}{T-t}, \frac{x_2}{T-t} \right) \quad (15)$$

is a solution of Eq. (11) with blow-up time T. This provides an accurate test for our numerical technique, because taking as initial data

$$E_0(x_1, x_2) = \frac{1}{T} \exp\left\{ i \frac{1}{T} \right\} \exp\left\{ -i \left(\frac{x_1^2 + x_2^2}{4T} \right) \right\} Q_r\left(\frac{x_1}{T}, \frac{x_2}{T} \right) \quad (16)$$

gives us a solution with exact blow-up time T, whereas, in the Gaussian case that we first considered, the blow-up time is not theoretically known (for more details, see [3, 24]). Moreover, it is shown in [25] that the solution E_ϵ of Eq. (11) computed with initial data $(1-\epsilon)E_0$ is global in time and converges to E when ϵ goes to 0. So, we compute solutions for $\epsilon = 0$, $\epsilon = 0.015$, $\epsilon = 0.02$, and $\epsilon = 0.05$ on a domain $\Omega =]-5, 5[\times]-5, 5[$ with $\Delta x_1 = \Delta x_2 = 0.1, \Delta t = 0.005$, and we chose $T = 1$.

The plot in Fig. 12 confirms the theoretical results. There is a blow-up for $\epsilon = 0$, and global solutions for $\epsilon > 0$. In addition, the smaller ϵ is, the closer the solution is symmetric with respect to $T = 1$. We can remark that the computed blow-up time seems to be less than 1, but, on the one hand, the mesh is too coarse to well represent the explosion, and, on the other hand, we see that the maximum value of the global solutions is reached close to 1 as ϵ goes to 0. However, the $1/|T-t|$ factor may not be the true increasing rate near the blow-up (for a very accurate study concerning this rate, see [27]). We plot in Fig. 13 the field amplitude for $\epsilon = 0.015$ at respective times $t = 0$ and $t = 2$. We see the symmetric aspect of the solution with respect to time $T = 1$, which shows that solution (15) is numerically satisfied.

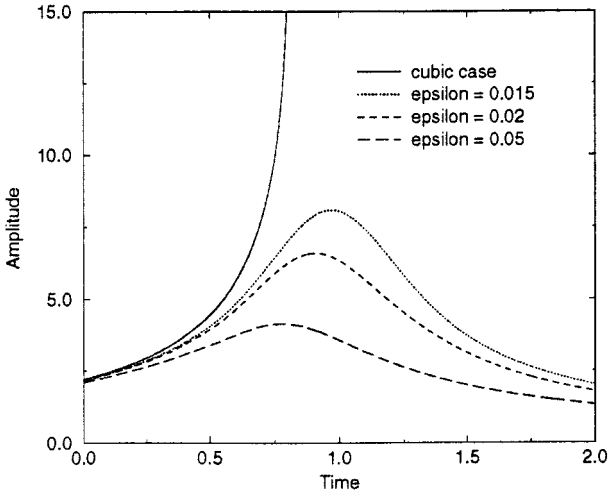

FIG. 12. Computation of the solution for different values of ϵ.

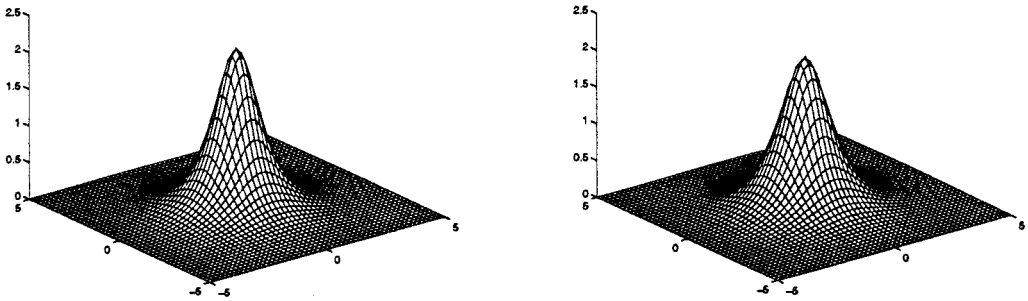

FIG. 13. Amplitude of the solution for $\epsilon = 0.015$: $t = 0$ and $t = 2$.

IV. MODIFIED NONLINEAR SCHRÖDINGER EQUATION

A. Physical Background

A new interesting situation occurs when very short and, hence, often powerful laser pulses are launched into a neutral medium: one can indeed experimentally observe new phenomena such as the formation of stable spatial structures like optical light bullets, for example, in the case of pulses launched into air ([4, 28]). To modelize such an effect, one can start from a Maxwell equation to describe the nonlinear propagation of the electric field E,

$$\left(\Delta - \frac{1}{c^2}\partial_t^2\right)(n_0 + \delta n)E = 0, \tag{17}$$

where, in Eq. (17), n_0 is the unperturbed refractive index of the medium, and δn is the perturbed one. Now assuming that an envelope approximation is possible (for a pulse with a long duration with respect to the time optical period and a typical spatial variation of the pulse electric field larger than the optical wavelength). We split E into amplitude u and phase Φ as $E = u\exp(i\Phi)$, and average Eq. (17) over the fast phase chosen as $\Phi = kz - \omega t$. We get a model equation of the nonlinear Schrödinger kind for the slowly varying complex amplitude $\bar{u}(\bar{r}, t)$:

$$(2ik\partial_z + \Delta_\perp)\bar{u}(r,\xi) + g(|\bar{u}(r,\xi)|^2)\bar{u}(r,\xi) = 0, \tag{18}$$

where $g(|\bar{u}|^2) \equiv 2k^2\delta n(|\bar{u}|^2/n_0)$ (neglecting terms in $(\delta n)^2$) and where $\xi = t - z/V_g$ stands for the propagation variable along the pulse taken along z, V_g being the pulse group velocity. The envelope approximation for u can be shown to remain valid even for short pulses (but generally longer than 100 fs) at moderate intensities (below a few 10^{14} W/cm^2) (see [29]). To derive Eq. (18), we have also neglected higher-order time derivatives such as $\beta_2\partial_\zeta^2$ and $\beta_3\partial_\xi^3$, respectively connected with pulse time compression and pulse broadening (since none of them are observed within the experimental resolution) by group velocity dispersion. Also, crossed time and spatial derivatives are discarded, as well the self-steepening process (unobserved) that would bring another contribution proportional to $-\partial_\xi|u|^2u$.

Equation (18) thus has only three terms: the first one describes the propagation, the second one accounts for possible diffraction effects, while the last term holds the relevant nonlinearities. The physical situation is the following: a short pulse is launched unfocused into the air. In a first zone, the dominant refractive index δn is given by the Kerr effect with a nonnegative coefficient $\delta n_K \equiv |E|^2$. After the beginning of Kerr collapse, the pulse is stabilized here, not by a natural saturating effect that would be in $\delta n'_K = -|E|^4$ coming from the next-order expansion of the index in the pulse power (an even expansion for centrosymmetric media), but by ionization of

the air; this is a rather subtle effect discussed elsewhere (see [30]). In fact, ionization occurs because the energy density becomes sufficient when the pulse radius shrinks enough, and this effect dominates the saturating four photon process in $|E|^4$ quoted above. There is a region where the two processes simultaneously happen. The free electrons liberated by the ionization process generate a plasma and add a contribution to the refractive index of the neutral medium:

$$\delta n_p = \left\{ 1 - \left(\frac{\omega_{pn}}{\omega}\right)^2 \frac{N_e(r,\xi)}{N_0} \right\}^{1/2} - 1 \simeq - \left(\frac{\omega_{pn}}{\omega}\right)^2 \frac{N_e(r,\xi)}{2N_0}, \qquad \omega_{pn}^2 = \frac{N_0 e^2}{m_{0e}\epsilon_0}. \tag{19}$$

We supposed here both a weak ionization and an underdense plasma, where $\omega_{pn}/\omega \ll 1$ (air is transparent for the wavelength of the incoming light). There is a single photoionization process that generates free electrons with a density N_e given by N_0 being the density of neutrals:

$$\partial_\xi N_e(r,\xi) = N_0 W(r,\xi) \tag{20}$$

$$\frac{N_e(r,\xi)}{N_0} = 1 - \exp\left\{ - \int_{-\infty}^{t} W(r,\xi')d\xi' \right\} \simeq \int_{-\infty}^{t} W(r,\xi')d\xi'. \tag{21}$$

W is the photoionization probability proportional to $|E|^{2p}$ for a multiphoton process, p being the number of absorbed photons. Considering an average ionization process with characteristic duration τ, which gives

$$\frac{N_e(r,\xi)}{N_0} \simeq \tau |E|^{2p}.$$

Note that the refractive index variation δn_p is a nonlinear function of intensity through Eqs. (20), (21) and is negative since W is nonnegative. In the case of air (mainly N_2 and O_2 molecules), we can choose an exponent $p = 9$ to match the experimental conditions at the working wavelength ($\lambda = 0.8$ nm) and the given values of the ionization first potentials for N_2 and O_2 (respectively, 12 and 15 eV). Thus, here the function g in Eq. (18) is the sum of the two relevant indexes $g = \delta n_K + \delta n_p$.

It can be shown that the competition between these two nonlinearities of opposite signs (here competing Kerr focusing and plasma ionization defocusing effects) is responsible for the stable observed structure (with soliton-like solutions, the second nonlinearity playing the role of the usual dispersion). It has also been possible to compute analytically the bullet characteristics (radius, energy density in the bullet, spectral feature) in good agreement with the experiments (see [30]).

B. Numerical Experiments

Motivated by the above-quoted physical situation, we now compute the solution of a modified nonlinear Schrödinger equation

$$i\partial_t E + \Delta_{x_1,x_2} E + |E|^2 E - \frac{b}{Q^{2p}} |E|^{2p} E = 0, \qquad p > 1, \tag{22}$$

where b and Q denote nonnegative constants. The value of p can be chosen on physical considerations as discussed above. However, in this part, we also feel free to set arbitrary values of p for numerical investigations. Note that, using Eq. (20), we should get an integral kernel for δn_p. However, we solve here a simplified model equation like Eq. (22), considering an instantaneous ionization with terms in $|E|^{2p}$ instead of $\int |E|^{2p}\, dt$. One can notice that other saturation mechanisms have been studied (see [31]), in a dissipative case for other physical backgrounds. The aim

here is to compute the approximate solution of this equation, with gaussian initial data

$$E_0(x_1, x_2) = qe^{-(x_1^2+x_2^2)}, \tag{23}$$

and to see the influence of the parameters b and p on the stabilization of the field intensity at the center of the domain. In what follows, we describe the time evolution of the electric field amplitude at the origin, computed on a domain $\Omega =]-5, 5[\times]-5, 5[$ with $\Delta x_1 = \Delta x_2 = 0.1, \Delta t = 0.001$, and the initial data (23) with $q = 4$.

1. Influence of b. First of all, we want to study the behavior of the solution in the physical case $p = 9$ with $Q = q = 4$. The plot in Fig. 14 shows that the field first behaves as if only anharmonic effects were taken into account, as it follows the solution for $b = 0$. But the attractive effect is counterbalanced by the higher-order term in Eq. (22), and a stationary state is reached. As we expect, the stabilization is more difficult to reach when the coefficient b is small: for $b = 5.10^{-10}$ (physical conditions in experiments), oscillations occur before stabilization.

We make in Fig. 15 a zoom of the field intensity with an ionization coefficient $b = 5.10^{-10}$ at initial time $t = 0$, and at time $t = 2.0$ when the field seems completely stabilized to a Gaussian equilibrium state. We point out that the radius of stabilization is much smaller than the initial one, which has been observed in optical experiments ([4]) and confirmed in [30]. This shows that the concentration feature of the field is kept during the stabilization regime. In this simulation, space steps have to be such that finite differences approximation of the partial derivatives remains valid, which means that a compromise must be chosen between $\Delta x_1, \Delta x_2$ and the coefficient b (which leads the concentration rate of the final stabilized state).

2. Special Case p = 2. This case allows us to study the competition between the two opposite effects in a different physical background than the one given in the beginning of this section by introducing a four-photon saturating process (that is $p = 2$ in Eq. (22)). We thus consider the

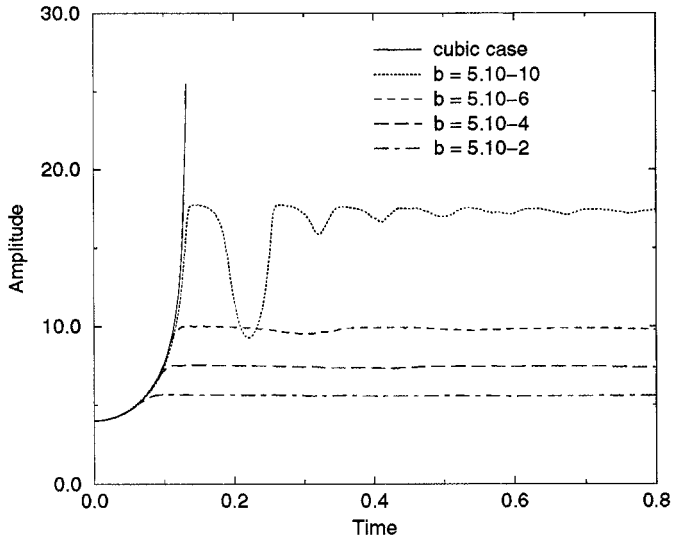

FIG. 14. Comparison of equilibrium stabilization.

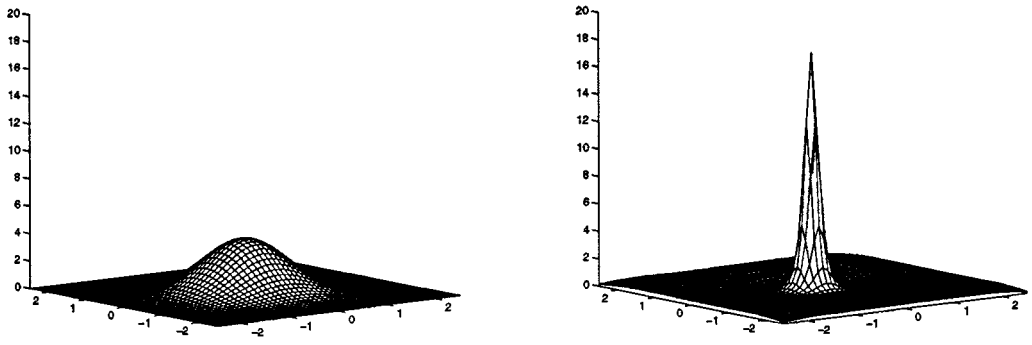

FIG. 15. Evolution of the field intensity at initial time and at time $t = 2.0$ ($b = 5.10^{-10}$).

equation

$$i\partial_t E + \Delta_{x_1,x_2} E + |E|^2 E - b|E|^4 E = 0 \tag{24}$$

for different values of b on a 100×100 grid (Fig. 16). We notice that the stabilization value decreases as b becomes larger to reach a stationary state for $b^* = 0.035$. Furthermore, for $b > b^*$, we observe the dispersion of the solution pointing out that the ionization term dominates. For $b = 1$, oscillations occur due to the interaction of the solution with the artificial boundary. But one should remember that absorbing boundary conditions are built for the linear case (see [2]). However, the amplitude goes to zero for large t.

Finally, we compute the solution of Eq. (24) for initial data (16) (still taken with $T = 1$) in order to evaluate the effect of the initial data on the behavior of the solution after the blow-up time of the solution given by Eq. (15). Figure 17 shows that, in this case, the behavior is similar to those obtained for the cubic equation by modifying the initial data (Fig. 12). Let us point out that the qualitative aspect of the solution after $T = 1$ is completely different for both initial data (23) and (16). The solution for the ground state as initial data can be seen as a limit case: here,

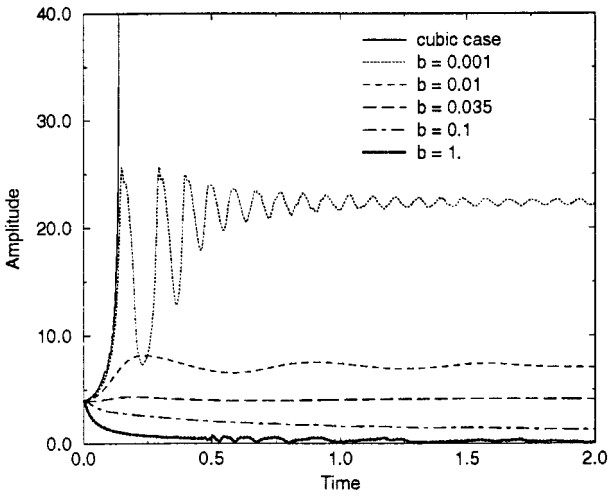

FIG. 16. Comparison of the solution for different values of b ($p = 2$).

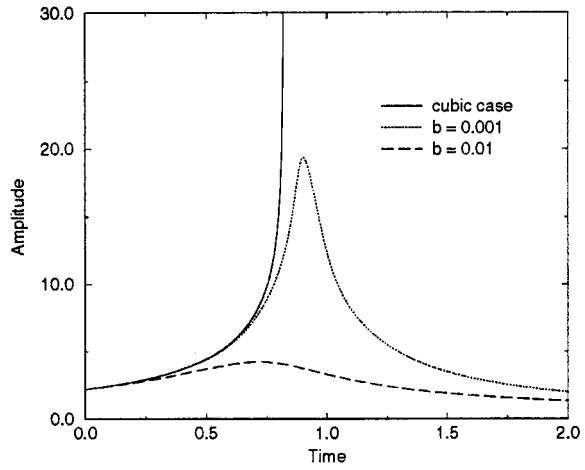

FIG. 17. Solutions computed with a ground state with different values of b.

when b goes to 0, the solution becomes symmetric with respect to $t = 1$ (and becomes close to the solution given by (15), see [3]), whereas profiles shown in Fig. 16 point out a stabilization once the higher-order nonlinear term comes into play, as physically predicted (see [30]).

V. RELATIVISTIC SYSTEM

We now apply our numerical procedure to a more complicated system. When the laser energy density I becomes of the order of 10^{18} W/cm^2 for a wavelength $\lambda \simeq 1$ μm, a new situation comes into play. The matter is fully ionized within less than an optical time cycle and the electrons should be treated relativistically, because the Lorentz factor for free electrons is modified. Indeed, using the formula $\gamma = 1/\sqrt{1-(v/c)^2}$, where v and c, respectively, denote the velocity of the particles in the plasma and the speed of light, we have $\gamma \simeq 2$ for $I \simeq 10^{18}$ W/cm^2.

A. Governing Model

We first rederive the relevant equations and then we compute the electric field (or the vector potential) evolution due to new nonlinear effects that are self-generated in the medium. The starting mathematical model consists in a nonlinear coupled relativistic system considering the Maxwell equations together with the hydrodynamics for the density n and the momentum p of the electrons. Here all these quantities depend on space variables (x, y, z) and time variable t. The relations between p and γ are

$$p = \gamma m_0 v, \qquad \text{or} \qquad \gamma^2 = 1 + \frac{p^2}{(m_0 c)^2}.$$

The Lorentz electromagnetic force on the electrons, introducing a quadripotential vector-potential (A, Φ), reads

$$F_L = q_e \left\{ -\frac{\partial A}{\partial t} - \nabla \Phi + v \times \text{curl } A \right\}.$$

Neglecting the pressure terms (low electronic temperature) and the ion motion on a short enough time scale, the hydrodynamical equations for electrons reduce to

$$\frac{\partial n}{\partial t} + \text{div}(nv) = 0, \tag{25}$$

$$\frac{\partial p}{\partial t} + (v \cdot \nabla)p = F_L. \tag{26}$$

Choosing a transverse vector potential $\bar{A} = |A_\perp| \exp i(kz - \omega t)\vec{e}_\perp$ with $\vec{e}_\perp \cdot \vec{k} = 0$ (valid for underdense plasmas $\frac{\omega_p}{\omega} < 1, \omega_p$ being the electronic plasma frequency) and averaging $(\langle\rangle)$ over the fast phase $\varphi = kz - \omega t$, the averaged Lorentz force yields the low frequency ponderomotive term $\langle F_L \rangle = -\nabla\langle\gamma\rangle m_0 c^2$. Now using the usual paraxial envelope approximation $|\frac{\partial^2}{\partial t^2} A_\perp| \ll |\omega \frac{\partial}{\partial t} A_\perp|$ and $|\frac{\partial^2}{\partial z^2} A_\perp| \ll |k \frac{\partial}{\partial z} A_\perp|$, we find the system of Eqs. (27) as in [8, 9]. Setting $n = n_0 + \delta n, V_g = \frac{d\omega}{dk}$, we get

$$\begin{cases} i\frac{\partial}{\partial z} A_\perp + \Delta_\perp A_\perp = -k_p^2 \left[1 - \frac{1}{\langle\gamma\rangle} - \frac{\delta n}{\langle\gamma\rangle n_0}\right], \\ \frac{\partial^2}{\partial t^2}\left(\frac{\delta n}{n_0}\right) + \frac{\omega_p^2}{\langle\gamma\rangle}\left(\frac{\delta n}{n_0}\right) = c^2 \nabla_\perp \cdot \left(\frac{\nabla_\perp \langle\gamma\rangle}{\langle\gamma\rangle}\right), \end{cases} \tag{27}$$

where the transverse Laplacian is defined by $\Delta_\perp A = \frac{\partial^2}{\partial x^2} A + \frac{\partial^2}{\partial y^2} A$, and the averaged Lorentz factor is approximated to second order by $\langle\gamma\rangle = (1 + d|A_\perp|^2)^{1/2}$, where d denotes a nonnegative constant depending on the wave polarization. The first equation of (27) includes the linear Schrödinger operator, and the space differential operators act only on $A_\perp$. On the right-hand side of (27), we find two nonlinearities: the relativistic mass nonlinearity $(\frac{1}{\langle\gamma\rangle} - 1)$ and the relativistic ponderomotive nonlinearity in $\frac{\delta n}{\langle\gamma\rangle n_0}$, where δn evolves according to the second equation of (27).

Considering the adiabatic limit of Eqs. (27) for the electronic density valid for $\omega_p \tau_0 \approx 1, \tau_0$ being the pulse duration, we get the saturated value for δn

$$\frac{\delta n}{n_0} = \langle\gamma\rangle \frac{\omega_p^2}{c^2} \nabla_\perp \cdot \left(\frac{\nabla_\perp \cdot \langle\gamma\rangle}{\langle\gamma\rangle}\right) \simeq k_p^{-2} \Delta_\perp \langle\gamma\rangle, \qquad k_p = \frac{\omega_p}{c},$$

and we find what can be called a relativistic nonlinear Schrödinger equation as

$$i\frac{\partial}{\partial z} A_\perp + \Delta_\perp A_\perp + k_p^2 \left[1 - \frac{1 + k_p^{-2}\Delta_\perp \gamma}{\gamma}\right] A_\perp = 0. \tag{28}$$

This equation has been much studied recently ([8, 9, 12, 32]), with $\max(0, 1 + k_p^{-2}\Delta_\perp \gamma)$ used in the nonlinear term in order to preserve the nonnegativity of the density. Furthermore, the mathematical analysis of Eq. (28) has been done in [33]: we know that the corresponding Cauchy problem has a unique solution in adapted functional spaces, assuming that the initial data is sufficiently small. But contrary to the nonlinear cubic Schrödinger Eq. (11), it is difficult to predict the evolution of the field when we consider large prescribed initial data, because of the fully nonlinear term involving the Laplacian of the Lorentz factor. In fact, in this case, Viriel techniques do not give as precise results as in the cubic case. However, in [32], it is shown that, if the initial field $A_{\perp,0}$ is chosen such that

$$H(0) = \int (|\nabla A_{\perp,0}|^2 - k_p^2(\gamma(A_{\perp,0}) - 1)^2 - |\nabla\gamma(A_{\perp,0})|^2)\, dx_1 dx_2 < 0,$$

there is no dispersion for the field amplitude. Here, we want to check the nondispersive case, to exhibit stationary solutions and localized ones.

B. Discretization of the Nonlinear Term

In these computations, we have to use a discretization of the nonlinear term, which respects the equation invariants M and H. As in the cubic case, we choose to keep the discrete conservation of the second invariant. Considering Eq. (28) at grid point indexed by (j,k) at time t_n, we use

$$\begin{aligned} h \;\equiv\; h^n_{j,k} = \frac{1}{|(A_\perp)^{n+1}_{j,k}|^2 - |(A_\perp)^n_{j,k}|^2} \Bigg\{ & \frac{1}{4\Delta x^2}(|\gamma((A_\perp)^n_{j+1,k}) - \gamma((A_\perp)^n_{j-1,k})|^2 \\ & - |\gamma((A_\perp)^{n+1}_{j+1,k}) - \gamma((A_\perp)^{n+1}_{j-1,k})|^2) \\ & + \frac{1}{4\Delta x_2^2}(|\gamma((A_\perp)^n_{j,k+1}) - \gamma((A_\perp)^n_{j,k-1})|^2 - |\gamma((A_\perp)^{n+1}_{j,k+1}) - \gamma((A_\perp)^{n+1}_{j,k-1})|^2) \\ & + \; k_p^2((\gamma((A_\perp)^n_{j,k}) - 1)^2 - (\gamma((A_\perp)^{n+1}_{j,k}) - 1))^2 \Bigg\}. \end{aligned}$$

Straightforward calculations based on multiplications with $(A_\perp)^n_{j,k} + (A_\perp)^{n+1}_{j,k}$ and $(A_\perp)^{n+1}_{j,k} - (A_\perp)^n_{j,k}$ and summation over all indexes j and k show the conservation of the invariants in that case.

C. Computations with Radial Initial Data

First, numerical tests have been made, with use of radial initial data (23). In this particular case, we find that, for a small prescribed value of k_p (for the tests, we chose $k_p = 1$), there is an increase of the field amplitude, linked to the initial amplitude profile. In Fig. 18, we view the amplitude at the center of the domain for several values of q.

It is interesting to point out that, whereas in the cubic equation with a nonlinearity $\beta|E|^2E$,

$$H(0) = 2q^2 \int (x_1^2 + x_2^2)\exp(-2(x_1^2 + x_2^2))\,dx_1dx_2 - \frac{\beta q^4}{4}\int \exp(-4(x_1^2 + x_2^2))\,dx_1dx_2 < 0$$

for a large value of either nonlinear coefficient β or field amplitude q, taking a big initial amplitude of the field does not yield a different behavior of the corresponding solution, for the relativistic case. Nevertheless, we can observe an increasing of the field amplitude for $q = 10$ until time $t = 0.5$. It is also interesting to point out that, for large values of q, we have $H < 0$, and there is no dispersion of $A_\perp$, which confirms the result given in [38]. But the lower bound for the field is numerically very small. Then, we solve numerically the stationary problem corresponding to Eq. (27), with $\Delta\gamma \equiv 0$, that is $\delta n \equiv 0$. Denoting by ω the corresponding frequency and considering a wavenumber $k_p = 1$, the equation is

$$-\omega u + \Delta u + \left\{1 - \frac{1}{\gamma}\right\} u = 0, \qquad \gamma = \sqrt{1 + |u|^2}. \tag{29}$$

In order to look for nonexistence of solutions of Eq. (29), it is convenient to use Pohozaev identities (see [1, 34]). In [36], a study of the stability of solitary waves for the relativistic Schrödinger equation has been made in the one-dimensional case. In the case of the bidimensional geometry, it is possible to show that there is no nontrivial solution of (29) for $\omega < 0$ and $\omega > 1$. Moreover, this result is optimal, since, for the complementary interval for the values of the frequency, a minimization theorem guarantees existence of radial solutions ([34]). As for the cubic case, we look for a radial stationary solution with use of a differential solver for the equation

$$\frac{1}{r}\frac{\partial}{\partial r}\left(r\frac{\partial}{\partial r}\right)U - \omega U + \left(1 - \frac{1}{\sqrt{1+U^2}}\right)U = 0,$$

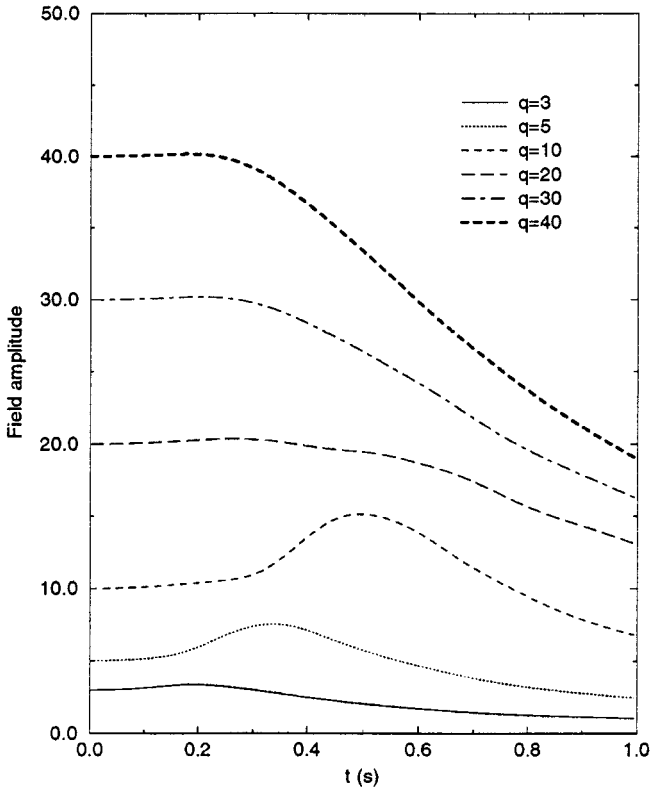

FIG. 18. Profile of the amplitude for different values of q.

with initial data $U(0) = 4.61536$ and $\frac{\partial}{\partial r}U(0) = 0$. The space domain is $\Omega =]-10, 10[\times]-10, 10[$, with space steps $\Delta x_1 = \Delta x_2 = 0.4$ and time increment $\Delta t = 0.01$. We plot in Fig. 19 the stationary profile U, and we view the amplitude evolution at the origin of the solution computed with U as initial data, compared with perturbed solutions taken with initial data $(1+\epsilon)U(\epsilon = 0.1, 0.05, -0.05, -0.1)$.

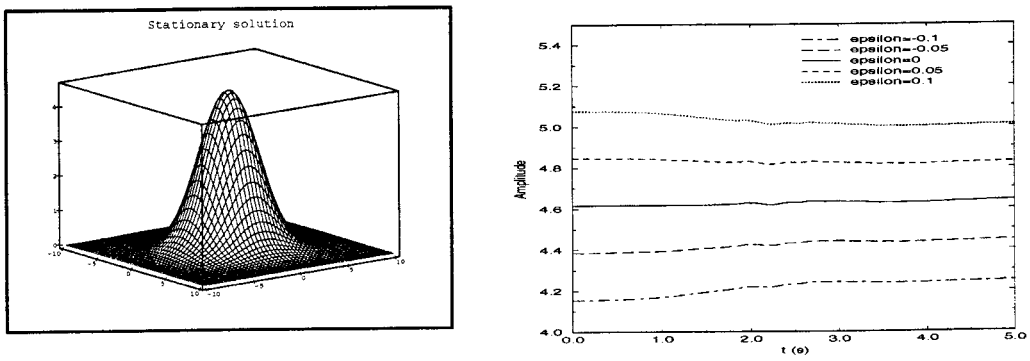

FIG. 19. Stationary profile and influence of amplitude perturbation.

We notice in this case that perturbations of stationary state do not affect the corresponding solution, as in the cubic case. In fact, starting the computations close to the stationary profile enables us to stay close to it.

The link between the two kinds of nonlinearities in Eq. (28) and in Eq. (11) can be expressed as follows: considering the solution $A_\perp$ of Eq. (28), and, assuming $|A_\perp| \ll 1$ and $\Delta_\perp \gamma \equiv 0$, we get

$$\left(1 - \frac{1 + k_p^{-2}\Delta_\perp \gamma}{\gamma}\right) A_\perp \equiv \frac{1}{2}|A_\perp|^2 A_\perp,$$

which leads to the nonlinear cubic Schrödinger equation. Thus, Eq. (28) can be seen as a generalization of Eq. (11) to the relativistic case. We reserve for future publication the analysis of the complete coupled set (27).

D. Computations with Other Initial Data

1. Numerical Tests with Azimutally Perturbed Initial Data We compute now the solution of Eq. (28) with the initial data

$$A_{\perp,0}(x_1, x_2) = \left\{1 + \epsilon r^2 \sum_{j=1}^{4} \cos(j\theta)\right\} \exp(-r^6), \text{where } (x_1, x_2) = (r\cos\theta, r\sin\theta). \quad (30)$$

The choice of Eq. (30) corresponds to an azimutal perturbation of a hypergaussian function ([9]). We took the following values of parameters: $\Delta x_1 = \Delta x_2 = 0.1, \Delta t = 0.00054, \epsilon = 0.01, d = 0.25$, and $k_p^2 = 522$. Figure 20 shows the profile of $A_\perp$ at respective times $t = 0$, and $t = 0.054$, showing the relativistic modification of the density. Final profile shows a filamentary structure of the field, and working with smaller space and time steps does not indicate a blow-up effect. At this time, one must be very careful, because radii of the filaments have the same order as the space step. This relativistic filamentation is of the same kind as the well-known classical filamentation in the cubic case (the two equations share filamentation properties).

2. Numerical Tests with Multiple Structures as Initial Data. The final test is devoted to the influence of boundary conditions on the filamentation process, as in the cubic case. For that, we consider an initial function taken as the superposition of four gaussian beams each traveling with

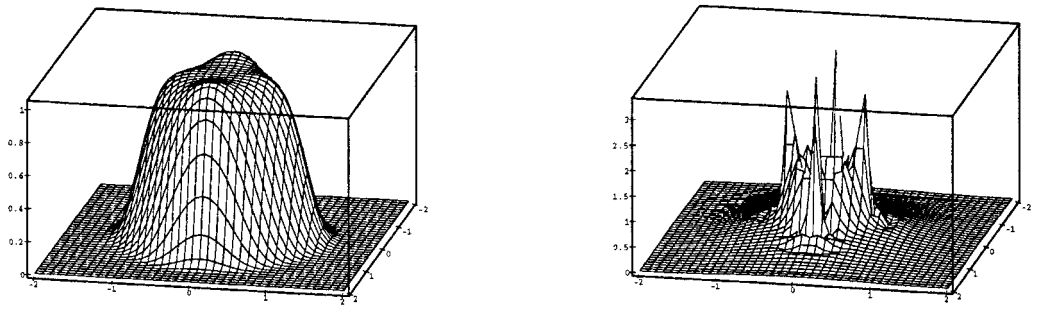

FIG. 20. Profiles of $A_\perp$ at times $t = 0$ and $t = 0.054$.

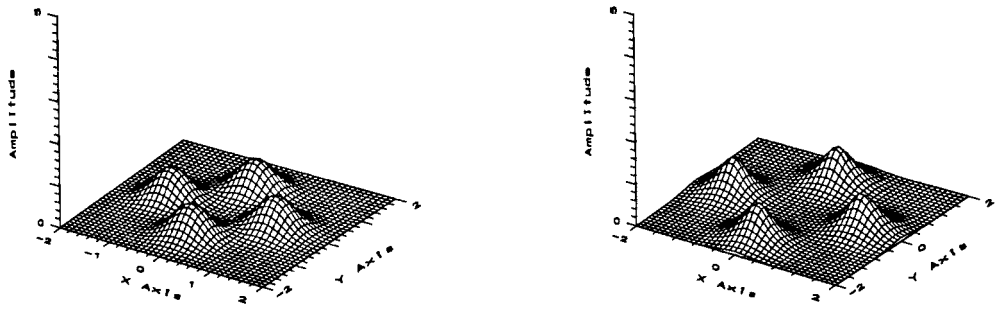

FIG. 21. Initial amplitude, amplitude at time $t = 0.02$ with absorbing conditions.

its own velocity, without radial term. We thus take

$$A_{\perp,0}(x_1, x_2) = \sum_{j=1}^{4} A_0^j \exp\{-\alpha_j((x - x_{j,1})^2 + (x_2 - x_{j,2})^2)\} \times \exp(i(k_{j,1}(x_1 - x_{j,1}) + k_{j,2}(x_2 - x_{j,2})),$$

where $A_j^0 = 0.75, k_{2,1} = k_{4,1} = k_{1,2} = k_{3,2} = 0, k_{1,1} = k_{2,2} = -k_{3,1} = -k_{4,2} = 6, \alpha = 5, x_{1,1} = x_{2,2} = -x_{3,1} = -x_{4,2} = x_{\max}/2$ and $x_{1,2} = x_{2,1} = x_{3,2} = x_{4,1} = 0$. This initial function has been chosen such that filamentation occurs after the four gaussian pulses have reached the boundary (to do so, we need to find a compromise between initial phase oscillations and amplitude). Nonlinear processes are such that each pulse evolves according to nonlinear effect, and also interacts with the other structures. The spatial grid parameters are the same as in the previous test, and we chose $\Delta t = 0.002$. Figures 21 and 22 show the initial amplitude and amplitude considered with absorbing conditions at time $t = 0.02, t = 0.06$, and $t = 0.18$, considered with $m = 19$. In Fig. 23 are plotted the fields, respectively, computed with Dirichlet conditions and with Neumann conditions at the same final time. Only absorbing conditions are give a right evolution in the numerical domain, while the two last conditions generate artificial filaments at the boundary, since the existing ones are trapped inside the domain, and also at the center because of the interaction process among the previous ones. This proves again the validity of our absorbing boundary conditions, even if small perturbations cannot be avoided due to the filamentation process.

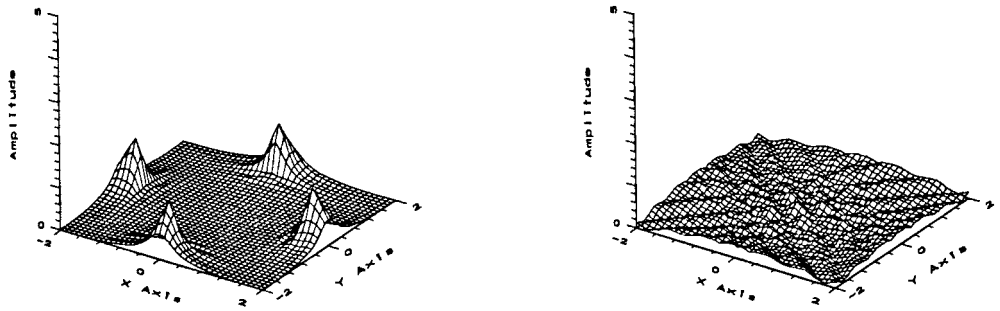

FIG. 22. Amplitude at time $t = 0.06$ and $t = 0.18$, absorbing conditions.

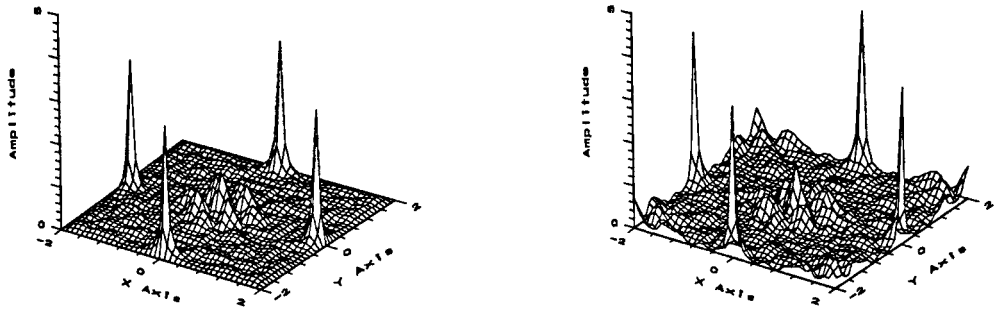

FIG. 23. Amplitude at time $t = 0.18$, Dirichlet conditions and Neumann conditions.

VI. CONCLUSIONS

We have implemented a new algorithm able to solve equations of the general type $i\partial_t a + \Delta_\perp a + f(|a|^2)a + g(\Delta_\perp a)a = 0$, with use of suitable absorbing boundary conditions. This also enables us to compute the solutions of Schrödinger equations without the need to choose the computational domain with respect to the predominant physical background (dispersion, concentration). Efficiency of our code has been shown for quite usual cases, where dispersive effects occur at the boundary. This method allows us to cover relevant nonlinear envelope equations important for plasma physics: the numerical simulations show with accuracy the behavior of various solutions. Moreover, computation of stationary states for both cubic and modified equations show the validity of the numerical method, providing an original numerical illustration of theoretical results given in [3, 25]. Finally, we have confirmed the existence of nontrivial stable structures in the case of both relativistic and modified ENLS equations as in agreement with what is observed experimentally.

The authors thank Prof. J.–C. Saut for valuable discussions and fruitful suggestions.

References

1. L. Di Menza, Ph.D. Thesis, University Bordeaux I, 1995.
2. L. Di Menza, ‘‘Transparent and absorbing boundary conditions for the Schrödinger equation in a bounded domain,’’ Numer Funct Anal Optimiz 18 (1997), 759–777.
3. F. Merle, ‘‘On uniqueness and continuation properties after blow-up time of self-similar solutions of nonlinear Schrödinger equation with critical exponent and critical mass,’’ Comm Pure Appl Math 45 (1992), 203–254.
4. A. Braun, G. Korn, X. Liu, D. Du, J. Squier, and G. Mourou, ‘‘Self-channeling of high-peak-power femtosecond laser pulses in air,’’ Opt Lett 20 (1995), 73–75.
5. A. V. Baskakov and V. A. Popov, ‘‘Implementation of transparent boundaries for numerical solutions of the Schrödinger equation,’’ Wave motion 14 (1991), 123–128.
6. T. M. Antonsen and P. Mora, ‘‘Self-focusing and Raman scattering of laser pulses in tenuous plasmas,’’ Phys Rev Let, 69 (1992), 2204–2207.
7. J. L. Bona, V. A. Dougalis, O. A. Karakashian, and W. R. McKinney, ‘‘Conservative, high-order numerical schemes for the generalized Korteweg-de Vries equation,’’ Phil Trans R Soc Lond A 351 (1995), 107–164.
8. A. B. Borisov, A. V. Borovskii, V. V. Korobkin, O. B. Shiryvaiev, X. M. Shi, T. S. Luk, A. McPherson, J. C. Solem, K. Boyer, C. K. Rhodes, ‘‘Observation of relativistic and charge-displacement self-channeling

of intense subpicosecond ultraviolet (248 nm) radiation in plasmas,'' Phys Rev Lett 68 (1992), 2309–2315.

9. A. B. Borisov, O. B. Shiryvaiev, A. McPherson, K. Boyer, and C. K. Rhodes, ''Stability analysis of relativistic and charge displacement self-channeling of intense laser pulses in underdense plasmas,'' Plasmas Phys Cont Fusion 37 (1995), 569–597.
10. A. V. Borovskii and A. L. Galkin, ''Dynamic modulation of an ultrashort high-intensity laser pulse in matter,'' Zh Eksp Teor Fiz., 104 (1993), 3311–3333.
11. H. S. Brandi, C. Manus, G. Manfray, and T. Lehner, ''Relativistic self-focusing of ultra intense laser pulses in plasmas,'' Phys Rev E 47 (1993), 3780.
12. P. Monot, T. Auguste, P. Gibbon, F. Jakober, G. Mainfray, A. Dulieu, M. Louis-Jacquet, G. Malka, and J. L. Miquet, ''Experiment demonstration of relativistic self-channeling of a multiterawatt laser pulse in an underdense plasma,'' Phys Rev Lett 74 (1995), 2953–2956.
13. M. Delfour, M. Fortin, G. Payre, ''Finite-difference solutions of a nonlinear Schrödinger equation,'' J Comp Phys 44 (1981), 277–288.
14. B. Engquist and A. Majda, ''Absorbing boundary conditions for the numerical simulation of waves,'' Math Comp 31 (1977), 629–651.
15. L. Halpern, Ph.D. Thesis, University Paris VI, 1980.
16. E. Dubach, ''Artificial boundary conditions for diffusion equation,'' J Comp Appl Math 70 (1996), 127–144.
17. A. Bamberger, B. Engquist, L. Halpern and P. Joly, ''High-order paraxial wave equation approximation in heterogeneous media,'' SIAM J Appl Math 48 (1988), 129–154.
18. F. Collino and P. Joly, ''Splitting of operators, alternate directions, and paraxial approximations for the three-dimensional wave equation,'' SIAM J Sci Comput 6 (1995), 1019–1048.
19. L. Halpern and L. J. Trefethen, ''Wide-angle one way wave equations,'' J Acoust Soc Amer 84 (1988), 1397–1404.
20. C.-H. Bruneau and L. Di Menza, ''Conditions aux limites transparentes et artificielles pour l'équation de Schrödinger en dimension l d'espace,'' C Rend Aca Sci 320, Ser I, 1 (1995), 89–95.
21. P. L. Sulem, C. Sulem, and A. Patera, ''Numerical simulation of singular solutions to the two-dimensional cubic Schrödinger equation,'' Comm Pure Appl Math 37 (1984), 755–778.
22. R. K. Dodd, J. C. Eilbeck, J. D. Gibbon, and H. C. Morris, Solitons and nonlinear wave equations, Academic, New York, 1982.
23. V. E. Zakharov, Theory of solitons, the inverse scattering method, Contemp Soviet Math (1968).
24. M. I. Weinstein, ''Lyapunov stability of ground states of nonlinear dispersive evolution equations,'' Comm Pure Appl Math 39 (1986), 51–68.
25. F. Merle, ''Limit behavior of saturated approximations of nonlinear Schrödinger equations,'' Comm Math Phys 149 (1992), 377–414.
26. M. I. Weinstein,''Nonlinear Schrödinger equations and sharp interpolation estimates,'' Comm Math Phys 87 (1983), 567–576.
27. B. Lemesurier, G. Papanicolaou, C. Sulem, and P. L. Sulem, Directions in PDE's, M. Crandall (Editor), Academic, New York, 1987.
28. J. Nibbering, P. F. Curley, G. Grillon, B. S. Prade, M. A. Franco, F. Salin and A. Mysyrowicz, ''Conical emission from self-guided femtosecond pulses in air,'' Opt Lett 21 (1996), 62–64.
29. G. P. Agrawal, Nonlinear fiber optics, Academic, New York, 1989.
30. T. Lehner, Formation of stable light bullets in air: competition between Kerr nonlinearity versus multi-photon ionization dynamics, to appear.

31. N. E. Kosmatov, V. F. Shvets, and V. E. Zakharov, ''Computer simulation of wave collapse in the nonlinear Schrödinger equation,'' Physica D 52 (1991), 16–35.

32. X. L. Chen and R. N. Sudan, ''Necessary and sufficient conditions for self-focusing of short ultraintense laser pulse in underdense plasma,'' Phys Rev Lett 70 (1993), 2082–2085.

33. A. De Bouard, N. Hayashi, and J. C. Saut, ''Global existense of small solutions to a relativistic nonlinear Schrödinger equation,'' C Rend Aca Sci 321, Ser I (1995), 175–178, and Comm in Math Phys 189 (1997), 73–105.

34. O. Kavian, Introduction à la théorie des points critiques et applications aux problèmes elliptiques, coll. Mathématiques et applications (SMAI), 13, Springer Verlag, 1991.

35. P. Sprangle, E. Esarey, J. Krall, and G. Joyce, ''Propagation and guiding of intense laser pulses in plasmas,'' Phys Rev Let 69 (1992), 2200–2203.

36. I. D. Iliev and K. P. Kirchev, ''Stability and instability of solitary waves for one-dimensional singular Schrödinger equations,'' Diff Int Equ 6 (1993), 687–703.